

Article citation info:

Wesołowski M, Ruchwa M, Dyyak I, Rucevskis S, Non-invasive and reliable approach for stiffness characterisation of 3D-printed plates, *Eksploracja i Niezawodność – Maintenance and Reliability* 2026; 28(1) <http://doi.org/10.17531/ein/207016>

## Non-invasive and reliable approach for stiffness characterisation of 3D-printed plates

Indexed by:



Mirosław Wesołowski<sup>a,\*</sup>, Mariusz Ruchwa<sup>a</sup>, Ivan Dyyak<sup>b</sup>, Sandris Rucevskis<sup>c</sup>

<sup>a</sup> Department of Structural Mechanics, Koszalin University of Technology, Poland

<sup>b</sup> Department of Applied Mathematics, Ivan Franko National University of Lviv, Ukraine

<sup>c</sup> Institute of Materials and Structures, Riga Technical University, Latvia

### Highlights

- CLPT effectively models 3D-printed multi-layered plate behavior.
- Contactless vibration analysis was conducted using a laser vibrometer.
- Validated FEM predictions align closely with experimental results.
- Inverse technique identifies 3D-printed plate stiffnesses non-invasively.

### Abstract

The additive manufacturing (3D printing) process of plates closely resembles the production of laminated composites. Both structures can be treated as multi-layered composites, where each layer may have distinct mechanical properties while forming an integrated structure. This study employs a non-destructive inverse technique based on dynamic tests to characterize the engineering constants (elastic parameters) of an individual printed layer. By using non-invasive experimental vibration tests (optical sensing), numerical modelling (SIMULIA/ABAQUS), and direct optimization processes (SIMULIA/Isight), the engineering constants of an individual printed layer are identified. A thin 3D-printed plate with a symmetric stacking sequence of layers is used for this characterization. The results are validated by predicting and measuring the dynamic response of a second symmetric plate with a different stacking sequence (printing orientations). The findings demonstrate that Classical Laminated Plate Theory (CLPT) can effectively predict the linear dynamic response of thin 3D-printed plates. Furthermore, the inverse technique is shown to be a robust and reliable method for determining the engineering constants of individual layers in a 3D-printed plate.

### Keywords

vibration test, laser vibrometer, 3D printing, inverse technique, FEM, engineering constants

This is an open access article under the CC BY license (<https://creativecommons.org/licenses/by/4.0/>)

### 1. Introduction

Fused Deposition Modelling (FDM) has become a widely adopted technique for producing plates and shell structures through 3D printing. In this process, components are created by depositing feedstock material layer by layer. In recent years, FDM has evolved beyond its original role as a prototyping method and is increasingly being used for manufacturing, enabling the production of components ready for immediate use.

The layered methodology employed in the production of 3D-printed plates is analogous to the fabrication of fibre-reinforced laminates. Specifically, similarities can be observed with the automated fibre placement production method [1,2]. Both processes involve the systematic deposition of material to create a highly tailored structure. In 3D printing, the application of a single filament path (line) directly corresponds to the

(\*) Corresponding author.

E-mail addresses:

M. Wesołowski (ORCID: 0000-0001-8909-6608) [mirosław.wesołowski@tu.koszalin.pl](mailto:mirosław.wesołowski@tu.koszalin.pl), M. Ruchwa (ORCID: 0000-0003-2260-8423) [mariusz.ruchwa@tu.koszalin.pl](mailto:mariusz.ruchwa@tu.koszalin.pl), I. Dyyak (ORCID: 0000-0001-5841-2604) [ivan.dyyak@lnu.edu.ua](mailto:ivan.dyyak@lnu.edu.ua), S. Rucevskis (ORCID: 0000-0002-0646-8064) [sandris.rucevskis@rtu.lv](mailto:sandris.rucevskis@rtu.lv)

deliberate placement of continuous fibres in laminates manufacturing. Furthermore, both processes allow precise control over the direction of material application in subsequent layers, enabling tailored anisotropic properties in the final structure. This ability to manipulate the orientation and arrangement of each layer is crucial for optimising mechanical performance and achieving desired structural characteristics in both 3D printed and laminated composite materials. These shared capabilities underscore the potential of leveraging Classical Laminated Plate Theory (CLPT) to predict and analyse the mechanical and dynamic responses of 3D-printed plates, as explored in [3, 4, 5].

Among the wide range of commercially available polymer-based filaments, those reinforced with short (chopped) carbon fibres are increasingly considered for industrial applications due to their enhanced mechanical performance. It is well established that incorporating short carbon fibres into a polymer matrix significantly improves stiffness and strength [6], especially in filaments based on polyamide matrices such as PA-6 and PA-12. For instance, in PA-12 filaments reinforced with short carbon fibres (CF-PA-12), the longitudinal stiffness can increase from approximately 1.0 [GPa] (pure PA-12) to 5.0–8.3 [GPa] after annealing [7]. As a result, CF-PA-12 is widely recognized for its high strength-to-weight ratio, heat resistance, and dimensional stability, making it suitable for high-performance industrial applications [8]. Typical uses include lightweight structural components such as brackets, housings, vibration- and heat-resistant parts, jigs, fixtures, tooling, fluid connectors (oil and gas), pumps, and drone frames. Its use is also promising in sandwich composite structures, particularly as an open-cell core material [9]. Given its broad industrial relevance, accurately understanding the mechanical behaviour – especially the stiffness – of CF-PA-12 is essential for selecting an appropriate numerical modelling strategy.

While the Classical Laminated Plate Theory (CLPT) offers a rational framework for modelling 3D-printed composite plates, accurately determining the engineering constants (i.e., elastic parameters) that underpin this theory remains challenging. These challenges primarily stem from the complex mesostructure and inherent anisotropy of 3D-printed materials [3, 10], both of which are highly sensitive to printing parameters such as raster angle [11, 12], layer thickness [13], deposition

strategy [14], void content [4, 11, 15], and build orientation [16]. To apply CLPT effectively, four engineering constants must be identified for each individual layer: longitudinal and transverse Young's moduli (relative to fibre orientation), Poisson's ratio, and the in-plane shear modulus. While these can theoretically be derived from elasticity theory [17], conventional tensile testing requires three to four different mechanical tests [5, 18] and a large number of printed samples to ensure reliability. As an alternative, computational material modelling – particularly using computational homogenization based on Finite Element Method (FEM) – has been employed to predict these constants. This method involves mesostructural modelling via a Representative Volume Element (RVE), often requiring micro-CT scanning to define the RVE geometry [19, 20]. Although this approach is accurate and efficient, it is computationally intensive and relies on an access to high-resolution imaging equipment. A comprehensive review of methods for determining elastic constants in 3D-printed structures is available in [21].

The present study aims to streamline the process of characterizing engineering constants by employing an inverse technique that integrates experimental data with numerical simulation. This well-established method, commonly used in the characterization of composite materials [22–24], has not yet been widely applied to 3D-printed plates. Rather than directly measuring elastic properties, the inverse technique identifies them indirectly by optimizing the match between experimentally measured dynamic characteristics and numerically simulated responses. This approach is specifically applicable to thin multi-layered plates, which is a key aspect of the study. Grounded in Classical Laminated Plate Theory (CLPT), the method ensures structural integrity while aligning 3D-printed material analysis with established composite material principles. The optimization process can be carried out iteratively [25, 26] or through response surface methodology [27, 28], reducing the experimental effort while maintaining accuracy in identifying key material parameters. To validate the proposed approach, the study conducts a comparative analysis by applying the derived engineering constants to predict the modal response of an additional 3D-printed plate. The predicted modal response is then compared with experimental observations, showing a strong correlation between them. This

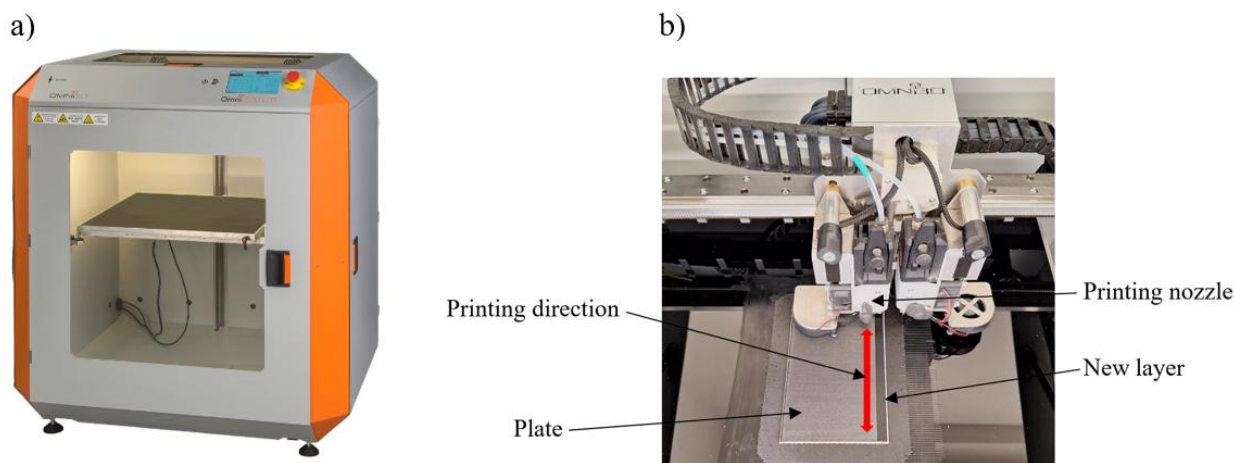


Fig. 1. a) 3D printing machine Omni 500 LITE, b) Printing process of a multi-layered plate

successful validation demonstrates the accuracy and reliability of the proposed approach. Furthermore, it highlights the effectiveness of combining advanced numerical modelling with experimental techniques to enhance our understanding of the dynamic behaviour and mechanical performance of 3D-printed structures.

## 2. Materials and Methods

### 2.1. 3D-printing process

The current study focuses on short carbon fibre reinforced polyamide 12 filament (a 15% of fibres content CF-PA-12, manufactured by IEMAI, China) used for thin plates fabrication. Assuming an analogy to laminated composites, the fibre orientation of an individual layer corresponds to the filament printing direction of the plate's layer (Fig. 1). The industrial 3D printing machine Omni 500 LITE was used for the manufacturing purpose.

The printing process of the plates must meet specific requirements to ensure they can be regarded as laminated composites, making them suitable for the application of CLPT. The main requirement is that there should be no gaps between filament lines after printing (Fig. 2). This ensures uniform transverse load distribution within each layer. Furthermore, all printed lines within a layer must be aligned in the same printing direction. Another key requirement is to achieve the lowest possible layer thickness, which reduces the effect of voids on the stiffness properties. To meet these requirements, the following printing process parameters were set: layer thickness of 0.2 [mm], nozzle diameter of 0.4 [mm], infill of 100 [%] (resulting in no filament gaps), infill pattern (printing direction)

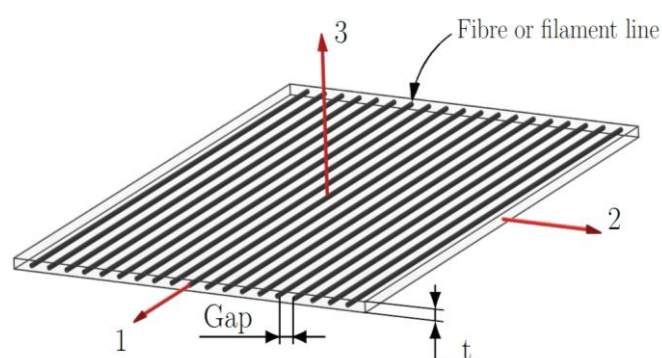


Fig. 2. Coordinate system and thickness of a single unidirectional layer.

of  $\pm\phi$  [deg] individually set for each layer (Fig. 3), nozzle temperature of 290.0 [°C], bed (printing table) temperature of 100.0 [°C], and closed chamber temperature of 50.0 [°C]. The CF-PA-12 filament was dried at a temperature of 60 [°C] for 4 hours before printing (WANHAO BOX 2 filament dryer). The printing process for the multi-layered plate samples is shown in Fig. 1. After the printing process, all the plates were annealed in a conventional oven at a temperature of 80 [°C] for 6 hours.

### 2.2. Numerical model

#### 2.2.1. The Classical Lamination Plate Theory (CLPT)

A concise overview of CLPT is provided to outline its fundamental features and highlight its applicability to the analysis of 3D-printed plates. For a more detailed and comprehensive explanation of CLPT, the references [29, 30] are recommended. Each unidirectional layer of the plate having a constant thickness  $t$  [mm], is considered orthotropic and subjected to a plane stress state. For a layer oriented in the 1-2 plane, as depicted in Fig. 2, the stress-strain relationship is given

by:

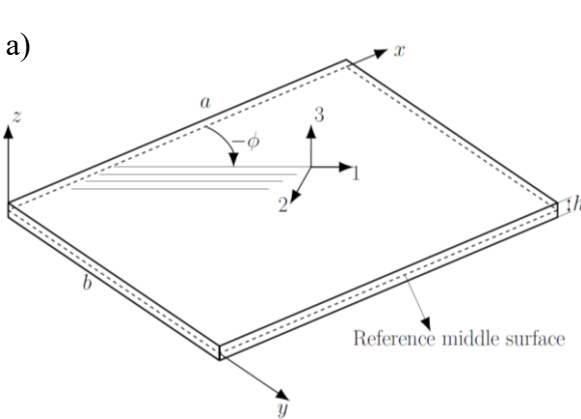
$$\begin{Bmatrix} \sigma_1 \\ \sigma_2 \\ \tau_{12} \end{Bmatrix} = \begin{bmatrix} Q_{11} & Q_{12} & 0 \\ Q_{12} & Q_{22} & 0 \\ 0 & 0 & Q_{66} \end{bmatrix} \begin{Bmatrix} \varepsilon_1 \\ \varepsilon_2 \\ \gamma_{12} \end{Bmatrix} \quad (1)$$

where  $\sigma_1, \sigma_2, \tau_{12}$  and  $\varepsilon_1, \varepsilon_2, \gamma_{12}$  are in plane stresses and strains respectively,  $Q_{ij}$  are reduced stiffnesses for the plane 1-2. The  $Q_{ij}$  are expressed in terms of engineering constants as:

$$Q_{11} = \frac{E_1}{1-\nu_{12}\nu_{21}}; Q_{22} = \frac{E_2}{1-\nu_{12}\nu_{21}}; Q_{12} = \frac{\nu_{12}E_2}{1-\nu_{12}\nu_{21}}; Q_{66} = G_{12}; \frac{\nu_{12}}{E_1} = \frac{\nu_{21}}{E_2} \quad (2)$$

where the  $E_1$  and  $E_2$  are longitudinal and transverse Young's moduli in the 1- and 2-directions (in the fibre direction and transverse direction, respectively, as shown in Fig. 2),  $G_{12}$  is the shear modulus in the 1-2 plane,  $\nu_{ij}$  are the Poisson's ratios. From the above, it can be inferred that there are four independent engineering constants which fully characterize the mechanical behaviour of the layer.

In common structural applications, composite plates are constructed by stacking multiple unidirectional layers oriented at different angles ( $\phi$ ) to create a multi-layered structure (Fig. 3(a)). In such cases, a transformation of the stress-strain relations from the layer coordinate system (1, 2, 3) to the global coordinate system (x, y, z) must be applied. The stress-strain relations for a layer in the x-y plane are as follows:



$$\begin{Bmatrix} \sigma_x \\ \sigma_y \\ \tau_{xy} \end{Bmatrix} = [\bar{Q}] \begin{Bmatrix} \varepsilon_x \\ \varepsilon_y \\ \gamma_{xy} \end{Bmatrix} = \begin{bmatrix} \bar{Q}_{11} & \bar{Q}_{12} & \bar{Q}_{16} \\ \bar{Q}_{12} & \bar{Q}_{22} & \bar{Q}_{26} \\ \bar{Q}_{16} & \bar{Q}_{26} & \bar{Q}_{66} \end{bmatrix} \begin{Bmatrix} \varepsilon_x \\ \varepsilon_y \\ \gamma_{xy} \end{Bmatrix} \quad (3)$$

where  $[\bar{Q}] = [T]^{-1}[Q][T]^{-T}$  and  $[T]$  being the transformation matrix.

For a multi-layered plate, the Eq. 1 and Eq. 3 can be considered as a stress-strain relations for the  $k^{\text{th}}$  layer. Thus the Eq. 3 can be written as:

$$\{\sigma\}_k = [\bar{Q}]_k \{\varepsilon\}_k \quad (4)$$

The primary objective of CLPT is to estimate the overall mechanical properties of a composite plate based on the characteristics of its individual layers, their stacking arrangement, and fibre orientations. This theory assumes that deformations are small enough to justify the linear elastic behaviour of the material. Additionally, it postulates that a line initially straight and normal to the mid-surface of the plate remains straight and perpendicular to the mid-surface during deformation. Furthermore, CLPT allows for reducing the three-dimensional problem to a two-dimensional problem of a deformable body (Fig. 3). The displacement field for CLPT is assumed to be as follows:

$$u = u_0 - z\alpha, \quad v = v_0 - z\beta, \quad w = w_0 \quad (5)$$

where  $(u_0, v_0, w_0)$  are the displacement components along the  $(x, y, z)$  coordinate directions of a point on a reference middle surface ( $z = 0$ ), respectively;  $\alpha = -\frac{\partial w_0}{\partial x}$ ,  $\beta = -\frac{\partial w_0}{\partial y}$ .

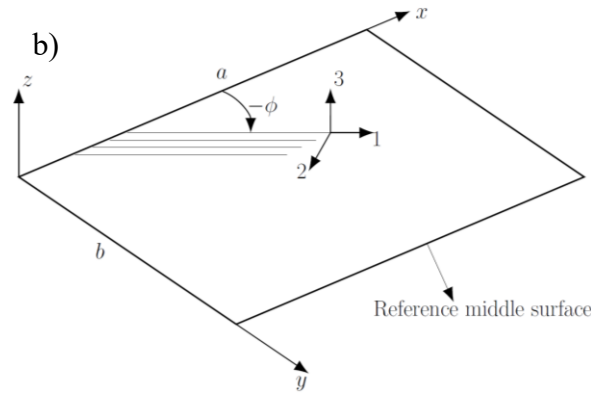


Fig. 3. (a) Geometrical characteristics of a 3D printed plate; (b) 2D representation of a plate.

The strains in terms of the assumed displacement field (Eq. 5)

are given as:

$$\begin{aligned} \varepsilon_x &= \frac{\partial u_0}{\partial x} - z \frac{\partial^2 w_0}{\partial x^2} \\ \varepsilon_y &= \frac{\partial v_0}{\partial y} - z \frac{\partial^2 w_0}{\partial y^2} \\ \gamma_{xy} &= \frac{\partial u_0}{\partial y} + \frac{\partial v_0}{\partial x} - 2z \frac{\partial^2 w_0}{\partial x \partial y} \end{aligned} \quad \text{Or in matrix notation:} \quad \begin{Bmatrix} \varepsilon_x \\ \varepsilon_y \\ \gamma_{xy} \end{Bmatrix} = \begin{Bmatrix} \varepsilon_x^0 \\ \varepsilon_y^0 \\ \gamma_{xy}^0 \end{Bmatrix} + z \begin{Bmatrix} \kappa_x \\ \kappa_y \\ \kappa_{xy} \end{Bmatrix} \quad (6)$$

where  $\varepsilon_x^0, \varepsilon_y^0, \gamma_{xy}^0$ , are middle surface strains;  $\kappa_x, \kappa_y$  and  $\kappa_{xy}$  are

bending and twisting curvatures of the middle surface,

respectively;  $z$  is a distance measured from the middle surface along thickness direction. The stresses in the  $k^{\text{th}}$  layer can now be expressed in terms of the plate's middle surface strains and curvatures as:

$$\begin{Bmatrix} \sigma_x \\ \sigma_y \\ \tau_{xy} \end{Bmatrix}_k = \begin{bmatrix} \bar{Q}_{11} & \bar{Q}_{12} & \bar{Q}_{16} \\ \bar{Q}_{12} & \bar{Q}_{22} & \bar{Q}_{26} \\ \bar{Q}_{16} & \bar{Q}_{26} & \bar{Q}_{66} \end{bmatrix}_k \begin{Bmatrix} \varepsilon_x^0 \\ \varepsilon_y^0 \\ \gamma_{xy}^0 \end{Bmatrix} + z \begin{Bmatrix} \kappa_x \\ \kappa_y \\ \kappa_{xy} \end{Bmatrix} \quad (7)$$

The constitutive equations of the multi-layered plate (or laminate) can be expressed in a contracted form [29]:

$$\begin{Bmatrix} N \\ M \end{Bmatrix} = \begin{bmatrix} A & B \\ B & D \end{bmatrix} \begin{Bmatrix} \varepsilon^0 \\ \kappa \end{Bmatrix} \quad (8)$$

where  $\{N\}$  and  $\{M\}$  are the in-plane force and moment resultants obtained by integrating the stresses in each layer through the plate thickness;  $[A]$ ,  $[B]$  and  $[D]$  are 3x3 matrices of extensional stiffnesses, bending-extensional coupling stiffnesses, and bending stiffnesses, respectively. The elements of the matrices  $[A]$ ,  $[B]$  and  $[D]$  are given as:

$$\begin{aligned} A_{ij} &= \sum_{k=1}^N (\bar{Q}_{ij})_k (z_k - z_{k-1}) \\ B_{ij} &= \frac{1}{2} \sum_{k=1}^N (\bar{Q}_{ij})_k (z_k^2 - z_{k-1}^2), \text{ for } i,j=1,2,6 \\ D_{ij} &= \frac{1}{3} \sum_{k=1}^N (\bar{Q}_{ij})_k (z_k^3 - z_{k-1}^3) \end{aligned} \quad (9)$$

where  $N$  is the total number of layers,  $z_k$  and  $z_{k-1}$  are the distances from the middle surface to the top and bottom of the  $k^{\text{th}}$  layer, respectively. The  $A_{ij}$ ,  $B_{ij}$  and  $D_{ij}$  represent the integrated stiffnesses of the multi-layered plate and depend on the layer stacking sequence, the fibre orientation angle ( $\phi$ ) (or printing direction), four engineering constants, and layer distance from the middle surface.

### 2.2.2. Finite Element Model

The Simulia/Abaqus software was used as a pre- and post-processor. A global (or body) coordinate system ( $x, y, z$ ) was located at the reference middle surface of the plate as given on Fig. 4. For each layer a lamina coordinate system (1, 2, 3) was defined with the direction 1 along the filament line of a layer. A printing direction ( $\phi$ ) of a single layer was defined between the  $x$ -axis and the 1-axis. The finite element (FE) method was used to develop a numerical model of the 3D printed multi-layered plate. The quadratic SR4 layered finite elements were used with orthotropic, linear elastic material model and following the CLPT. All edges of the plate's model were free of any boundary conditions (no supports – FFFF). The scope of the current study requires the model to undergo normal mode

analysis (Frequency analysis type in the Simulia/Abaqus) to extract numerical eigenfrequencies and eigenvectors (mode shapes). The eigenvalue problem for undamped free vibrations is represented as:

$$(\mathbf{K} - \omega_n^2 \mathbf{M}) \Phi_n = \mathbf{0} \quad (10)$$

where  $\mathbf{K}$  and  $\mathbf{M}$  are the stiffness and mass matrices of the plate, respectively;  $\Phi_n$  are the  $n^{\text{th}}$  eigenvectors of the corresponding eigenvalues  $\omega_n = 2\pi f_n^{FEM}$ , where  $f_n^{FEM}$  are eigenfrequencies. The normal mode analysis was conducted using the Lanczos mode-extraction method, and the eigenvalues and corresponding eigenvectors of the FFFF plate were determined.

### 2.3. The inverse technique

In the current study, an inverse method combining experimental vibration testing and direct optimization is used to determine the four engineering constants of a single layer of a 3D-printed thin plate. Initially, trial values for the engineering constants, which are the parameters to be identified, are assigned to initiate the FEM analysis for extracting eigenfrequencies and eigenvectors. A laser-based vibration test is conducted once to obtain the experimental resonant frequencies. The optimization of the engineering constants is then performed using Simulia/Isight by minimizing the objective function, which represents the relative error between the experimental dataset and the numerical results:

$$\theta(\mathbf{x}) = \sum_{n=1}^I \left[ \frac{(f_n^{EXP})^2 - (f_n^{FEM})^2}{(f_n^{EXP})^2} \right]^2 \quad (11)$$

where  $f_n^{EXP}$  are the experimentally determined resonant frequencies;  $f_n^{FEM}$  are the numerically calculated eigenfrequencies;  $\mathbf{x}$  is the vector of unknown parameters;  $I$  is the total number of eigenfrequencies (resonances) considered in the analysis. To minimise the objective function, the following optimisation problem was solved:  $\min \theta(\mathbf{x})$ , subjected to constraints  $\mathbf{x}_i^L < \mathbf{x}_i < \mathbf{x}_i^U$ , where  $\mathbf{x} = [\mathbf{x}_1, \mathbf{x}_2, \mathbf{x}_3, \mathbf{x}_4] = [E_1, E_2, G_{12}, \nu_{12}]$ ,  $\mathbf{x}_i^L$  and  $\mathbf{x}_i^U$  are lower and upper limits of the identification parameters, respectively. The Hooke-Jeeves optimisation method was used to find an optimal unknown vector  $[\mathbf{x}]$ . It shall be noted that the objective function is constructed in such a way, to account for multiple eigenfrequencies resonances to be considered simultaneously. The optimization procedure is carried out iteratively until a specified convergence criterion ( $\mu$ ) is met.

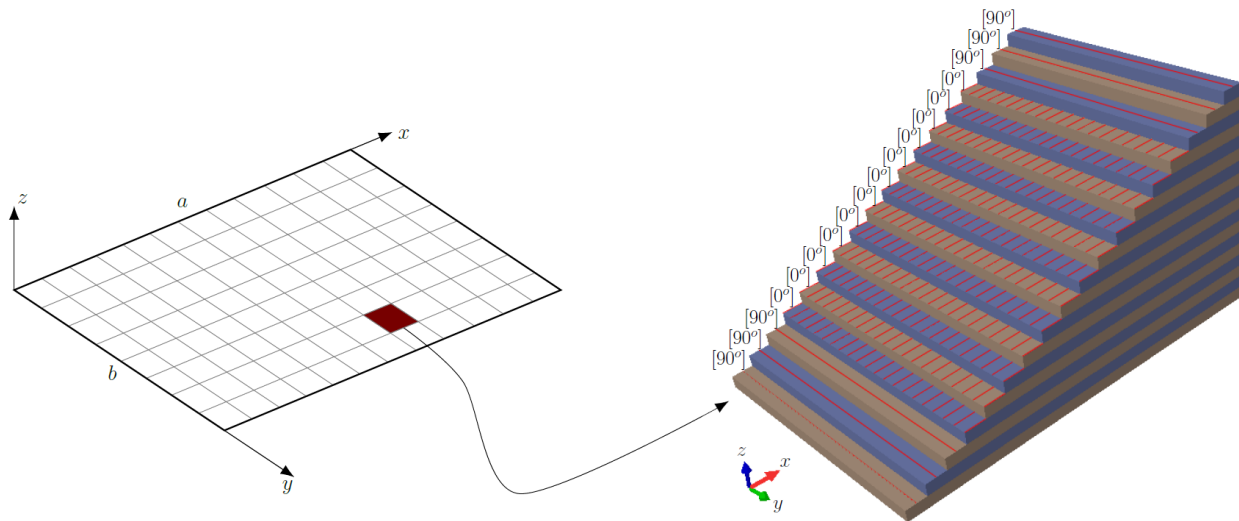


Fig. 4. FEM model and layers stacking sequence of the Plate 1.

### 2.3.1. Hooke-Jeeves optimisation method

The Hooke-Jeeves optimization method (also known as the Hooke-Jeeves Pattern Search Method) is a derivative-free, direct search algorithm used for nonlinear optimization problems, particularly when derivatives are difficult or expensive to compute. It was developed by Robert Hooke and T.A. Jeeves in 1961 [31]. This method is well suited for simulation-based optimization (i.e., finite element models) and relies on a specific search strategy known as Pattern Search (PS). PS is a direct search routine that minimizes the objective function  $\theta(\mathbf{x})$ , where the argument  $\mathbf{x}$  varies until the minimum of  $\theta(\mathbf{x})$  is found. The successive values of  $\mathbf{x}$  are interpreted as points in a K-dimensional space. The transition from one point (i.e., the current vector of unknown parameters) to the next is called a move. A move is considered successful if  $\theta(\mathbf{x})$  decreases; otherwise, it is a failure. The PS routine includes two types of moves. The first is an exploratory move, designed to gather information about the behaviour of  $\theta(\mathbf{x})$ . This information is inferred solely from the success or failure of exploratory moves, without relying on the magnitude of the objective function values. The basic success/failure feedback is then combined into a pattern that suggests a likely direction for a successful move. The exploratory moves form a (vector) basis for the argument space. Starting from an initial point  $\mathbf{x}$ , the algorithm varies each variable by a step size of  $\pm\Delta$  to check for improvements in  $\theta(\mathbf{x})$ . If improvement is found, the algorithm proceeds to that new point. If not, the step size is reduced. This reduction continues until  $\Delta < \mu$ , where  $\mu$  is a predefined

convergence or termination criterion.

### 2.4. Experimental procedure

An experimental investigation play a crucial role in the proposed approach for identifying engineering constants. It is essential to design the vibration testing methodology in a way that minimizes the adverse effects of the testing apparatus on the measured resonance frequencies. Specifically, this involves mitigating the influence of additional mass introduced by measurement sensors and exciters, which can distort the experimental results relative to the computed eigenfrequencies. Consequently, experimental modal analysis was conducted using an optical vibrometer (POLYTEC Scanning Laser Vibrometer PSV-400-B), which enables contactless, multi-point (scanning) vibration measurement. The experimental setup, along with the individual components of the PSV-400-B system, is shown in Fig. 5. The PSV-400-B functions based on the Doppler effect, measuring frequency variations in the backscattered light wave from a vibrating surface of a plate. When a wave reflects off a vibrating plate and is detected by a laser vibrometer, the observed frequency shift can be mathematically expressed as:

$$f_D = \frac{2 \cdot v}{\lambda} \quad (12)$$

where  $v$  represents the object's velocity and  $\lambda = 633$  [nm] denotes the emitted wave's wavelength. To determine an object's velocity, the Doppler frequency shift must be recorded at a known wavelength, a task accomplished through a laser interferometer. Optical interference requires two coherent light

waves, with their respective intensities  $I_r$  and  $I_m$ , to overlap. The resulting intensity is modulated according to the following equation:

$$\Gamma = I_r + I_m + 2\sqrt{I_r I_m} \cdot \cos \left[ \frac{2\pi(s_r - s_m)}{\lambda} \right] \quad (13)$$

where  $\Gamma$  is an interference term and is associated with the path length difference between the two laser beams;  $I_r$  and  $I_m$  correspond to the intensities of the reference and measurement laser beams, respectively;  $s_r$  and  $s_m$  represent the respective path lengths [32]. The optical path of the laser light (beam) is shown on Fig. 6 and it is enclosed in the scanning head of the PSV-400-B system. A helium-neon laser beam is initially divided by Beam Splitter 1, producing both a reference beam and a measurement beam. The measurement beam continues through Beam Splitter 2, where it is directed onto the test object. Upon striking the surface, the beam is reflected and subsequently redirected downward by Beam Splitter 2. This reflected beam is then combined with the reference beam at Beam Splitter 3 and guided toward a photo detector (VD-07). Since the reference beam's path length remains stable over time, the vibrations of the examined object result in a characteristic fringe pattern (alternating bright and dark bands) on the detector, a phenomenon typical of interferometry. Each complete dark-bright transition in the fringe pattern corresponds to a displacement equal to half the wavelength of the laser light used. Given that helium-neon lasers are predominantly employed in vibrometry, this displacement is approximately  $\lambda/2$ . Variations in the optical path length over time induce Doppler frequency shifts in the measurement beam, allowing precise detection and analysis of the object's vibrational behaviour. This implies that the modulation frequency of the interferometric pattern is directly correlated with the object's velocity. However, since movement away from the interferometer produces an identical interference pattern and frequency shift as movement toward it, To address this limitation, an acousto-optic modulator (Bragg Cell) is introduced into the reference beam path. This

modification enables not only the measurement of vibration amplitude but also the identification of its direction. this configuration is unable to determine the vibration direction of the object.

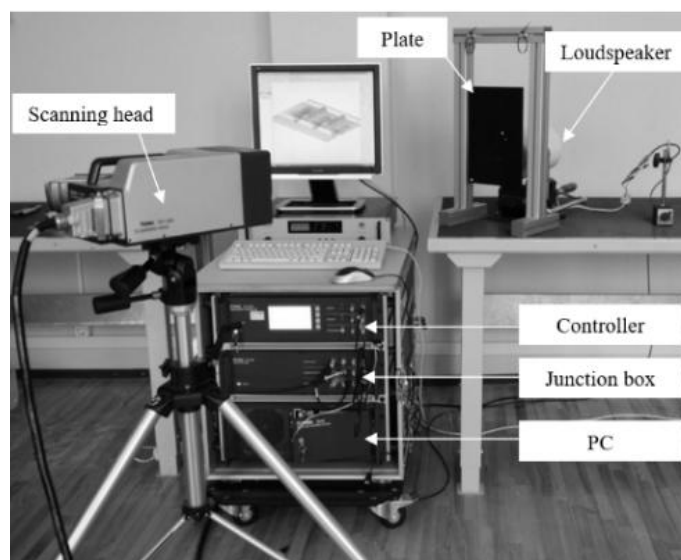


Fig. 5. Experimental setup.

The entire process described above is repeated for all predefined measurement points, which are evenly distributed across the surface of the examined object. The measurement points are defined based on image correlation using a camera integrated into the scanning head. The laser beam is automatically directed to successive measurement points (scanning) via optical mirrors. Upon completion of the measurements at each point, the averaged Frequency Response Function (FRF) and vibration mode shapes are obtained. The FRF is then used to extract the resonance frequencies based on the Peak-Picking method [33]. In order to achieve a complete non-invasive measurement procedure, the plates were driven to vibration through a modal loudspeaker with a periodic chirp signal spanning in a desired frequency range. The signal was provided via the internal signal generator of the PSV-400-B system. In addition, a free boundary conditions of the plates were ensured by suspending the plates using two thin nylon threads affixed to their upper corners.

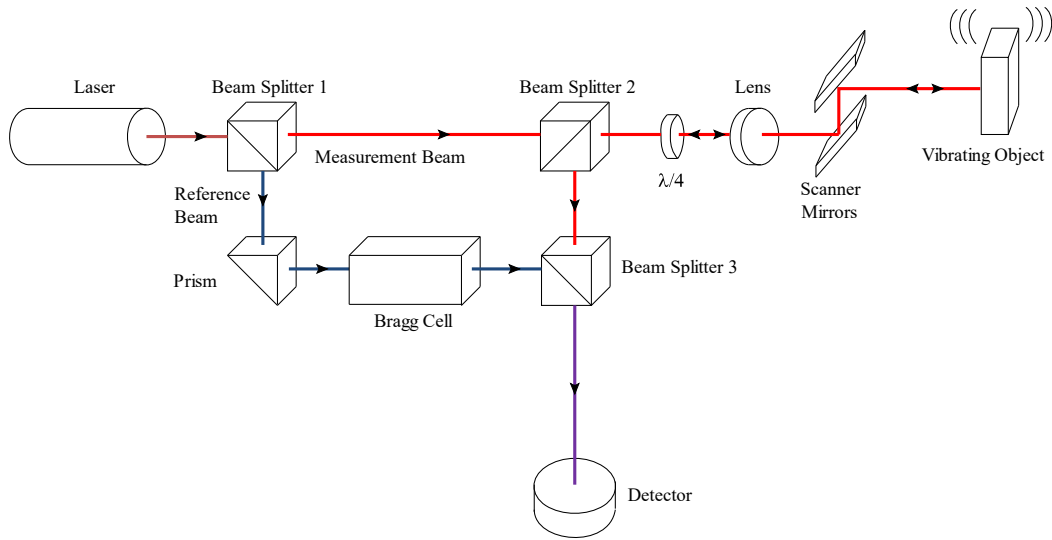


Fig. 6. Optical path of a laser beam.

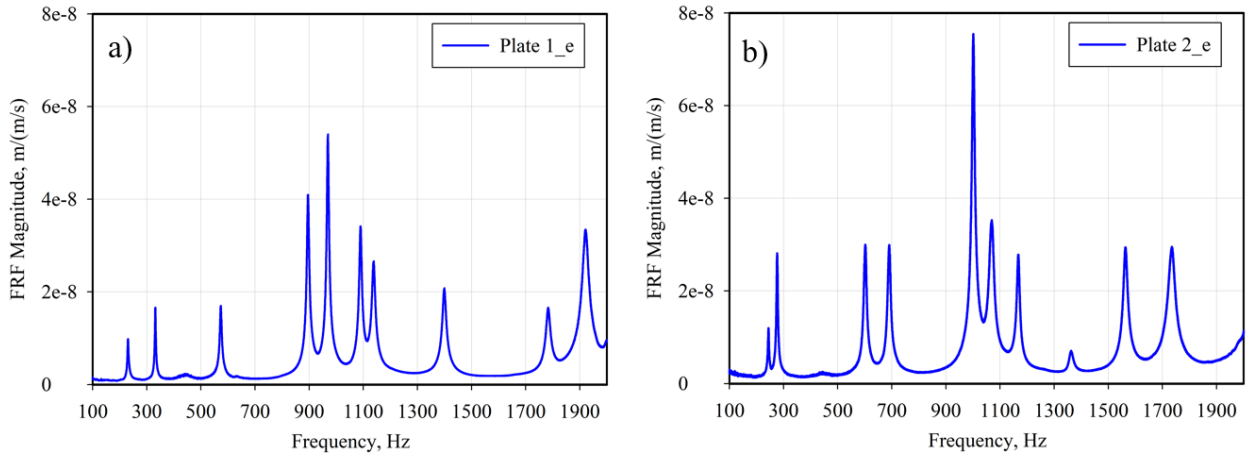


Fig. 7. Examples of the Frequency Response Functions: a) Plate 1; b) Plate 2.

### 3. Results

#### 3.1. Identification example

An identification case was performed with a purpose to characterise four elastic constants (elastic parameters) of a 3D printed plates:  $E_1$ ,  $E_2$ ,  $G_{12}$ ,  $\nu_{12}$ . Two types of plates were developed by 3D printing process with symmetric stacking sequence: Plate 1 with a stacking sequence  $[90_3/0_6]_s$  and Plate 2 with a stacking sequence  $[90_3/-45/45/-45_2/45/-45]_s$ . The geometric characteristics of the plates are given on Fig. 3(a) and listed in Tab. 1. Plate 1 was used for the identification purpose, while Plate 2 was used for the results validation. For statistical analysis, five samples of each plate were printed and subjected to experimental vibration tests. The dynamic tests were performed aiming for resonant frequencies and mode shapes extraction. The FRFs of the plates were stored (Fig. 7) and the first 10 resonances (maximum peaks) and mode shapes within

the frequency range of 0 to 2000 [Hz] were extracted. The obtained resonances and their averaged values are given in Tab. 2 and Tab. 3. The averaged values of Plate 1 served as input experimental responses ( $f_n^{EXP}$ ) in the inverse problem. In order to verify the repeatability of the measurements the Coefficient of Variation was calculated for each resonance as [34]:

$$CV = \frac{S_{n-1}}{\bar{x}} * 100 \quad (14)$$

where  $S_{n-1}$  is a standard deviation,  $\bar{x}$  is an average value.

Next, two models of 3D-printed multi-layered plates were developed according to their stacking sequence used in the 3D-printing process. The layer breakdown view of a plate model is shown in Fig. 4, with the first layer counted from the bottom of the plate. Frequency analysis was set up in the range of 0 to 2000 [Hz] for the models to extract numerical eigenfrequencies and eigenvectors. The geometric characteristics of the plate models were consistent with those of the 3D-printed plates and

are listed in Table 1. The material density, as well as the trial elastic properties required to run the initial analysis, were set as given in Table 4. Before proceeding with the optimization process, the convergence of the FEM solution (eigenfrequencies) was studied. The satisfactory convergence was achieved with 3750 elements for all studied mode shapes (Fig. 8).

After acquiring experimental and numerical data, the inverse problem for Plate 1 was defined. The Simulia/Isight software was used to develop the procedure with the objective function constructed according to Eq. 11. A schematic view of the

iterative procedure is shown in Fig. 9(a). The vector of the unknown parameters was defined as:  $\mathbf{x}=[\mathbf{x}_1, \mathbf{x}_2, \mathbf{x}_3, \mathbf{x}_4]=[E_1, E_2, G_{12}, \nu_{12}]$ . The following lower and upper limits for the engineering constants were used:  $7.5 < E_1 < 9.9$  [GPa],  $1.5 < E_2 < 2.5$  [GPa],  $0.75 < G_{12} < 0.96$  [GPa],  $0.40 < \nu_{12} < 0.5$ . The Hooke-Jeeves optimisation method with the convergence criterion  $\mu = 1.0 * 10^{-6}$  was run. The optimal unknown vector was found after 60 iteration (Fig. 9(b)). The optimal values of the engineering constants are given in Tab. 5.

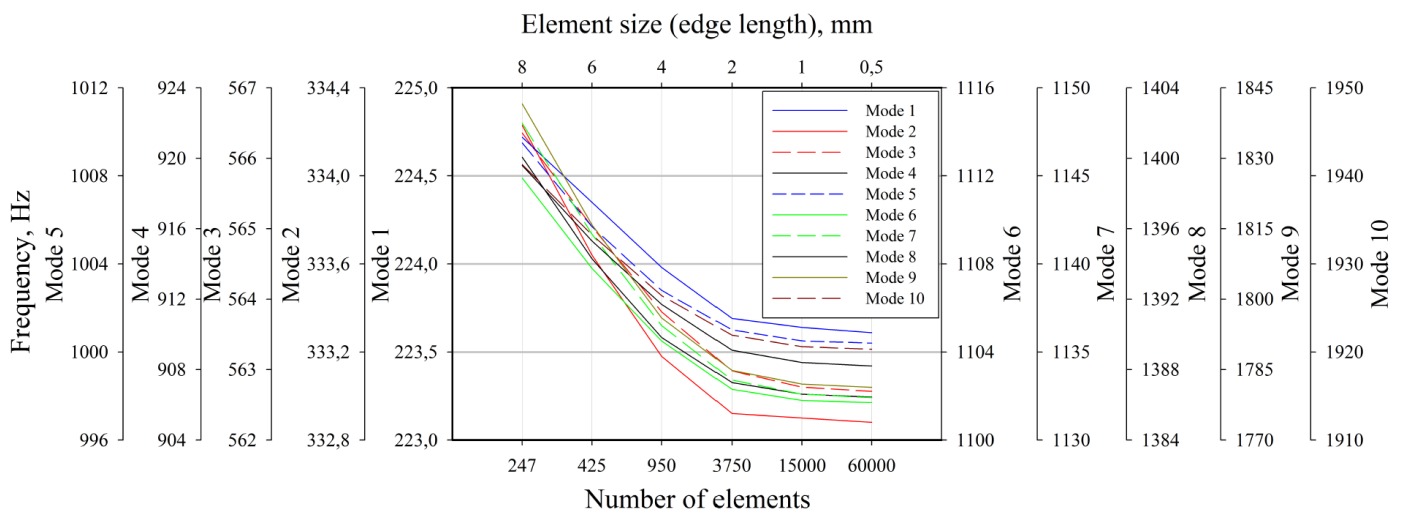


Fig. 8. Convergence study for the eigenfrequencies (Hz) versus quadratic finite elements' size.

Tab. 1. Geometrical characteristics of the 3D printed plates.

	a, [mm]	b, [mm]	h, [mm]	t, [mm]	No. of layers
Plate 1	150.00	100.00	3.60	0.20	18
Plate 2	150.00	100.00	3.60	0.20	18

Tab. 2. Results of the vibration tests for the Plate 1 –  $[90_3/0_6]_s$ .

	Plate 1_a	Plate 1_b	Plate 1_c	Plate 1_d	Plate 1_e	$\bar{x}$	CV
Resonance (n)	[Hz]						[%]
1	224.69	220.47	218.13	222.66	230.94	223.38	2.19
2	335.94	334.53	332.66	329.84	331.88	332.97	0.71
3	565.64	559.38	553.91	558.75	573.75	562.29	1.36
4	911.82	911.72	905.31	900.78	896.63	905.25	0.74
5	999.84	1009.46	1009.78	1001.4	969.69	998.03	1.65
6	1104.78	1107.47	1108.43	1106.42	1091.25	1103.67	0.64
7	1143.78	1138.68	1130.68	1132.58	1138.98	1136.94	0.47
8	1397.67	1394.56	1389.78	1384.89	1399.43	1393.27	0.43
9	1786.78	1784.68	1773.87	1775.58	1781.85	1780.55	0.32
10	1937.26	1925.46	1915.21	1922.24	1919.53	1923.94	0.43

Tab. 3. Results of the vibration tests for the Plate 2 –  $[90_3/-45/45/-45_2/45/-45]_s$

	Plate 2_a	Plate 2_b	Plate 2_c	Plate 2_d	Plate 2_e	$\bar{x}$	CV
Resonance (n)	[Hz]						[%]
1	243.49	242.56	243.79	241.67	244.12	243.13	0.41
2	278.75	277.65	278.27	276.41	276.34	277.48	0.39
3	605.46	604.21	605.31	602.34	601.80	603.82	0.28
4	691.87	689.13	693.82	689.38	690.30	690.90	0.28
5	1013.28	1013.91	1012.50	1003.58	1000.79	1008.81	0.61
6	1085.56	1081.56	1085.47	1080.32	1070.56	1080.69	0.57
7	1167.13	1165.16	1164.38	1158.46	1167.78	1164.58	0.32
8	1358.94	1352.56	1359.45	1350.64	1363.47	1357.01	0.39
9	1564.78	1560.78	1561.46	1551.46	1562.34	1560.16	0.33
10	1746.25	1737.28	1744.87	1733.68	1735.76	1739.57	0.32

### 3.1. Results validation

To validate the reliability of the identified elastic properties, the FEM model of the plate was modified to account for the new stacking sequence of Plate 2. The identified engineering constants (Tab. 5) were used to predict the numerical dynamic parameters (eigenfrequency and eigenvectors). The numerical results were then compared with the corresponding experimental data for mode shapes (Tab. 6) and resonances (Tab. 7) of Plate 2. The good agreement between the results can be observed from the given data.

### 4. Discussion

The elastic constants  $E_1$ ,  $E_2$ ,  $G_{12}$ ,  $\nu_{12}$  of an individual 3D-printed layer were successfully identified using an inverse technique. The method demonstrated strong efficiency and robustness, achieving rapid convergence in the optimization process within just 60 iterations. High repeatability in both sample fabrication and vibration measurements was confirmed by low Coefficient of Variation (CV) values across tested plates. The non-invasive testing approach produced high-quality Frequency Response Functions (FRFs), enabling precise extraction of the plates' resonant frequencies.

The identified engineering constants were then used to numerically predict the dynamic parameters of Plate 2, which featured a different stacking sequence than Plate 1. Both eigenfrequencies and eigenvectors showed excellent agreement with experimental results, with an average relative error of only 0.92%. A key outcome of the study is the ability to tailor the elastic properties of multi-layered 3D-printed plates using the

constants of individual layers and Classical Laminate Plate Theory (CLPT). This capability offers a solid foundation for the structural design and optimization of 3D-printed composites.

Notably, the printed layer – with no gaps between adjacent lines – exhibited approximately 15% higher stiffness than the filament alone. This enhancement is attributed to fibre bridging and interfacial continuity, which improve load transfer between lines. Interdiffusion of the polymer matrix and partial fibre entanglement at the interfaces increase cohesion, enabling more efficient stress distribution and improved mechanical performance. Future studies using X-ray computed tomography will allow for a more accurate assessment of this phenomenon.

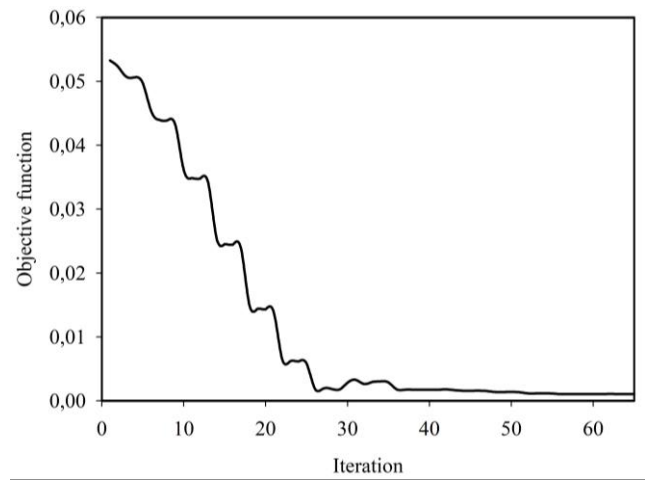
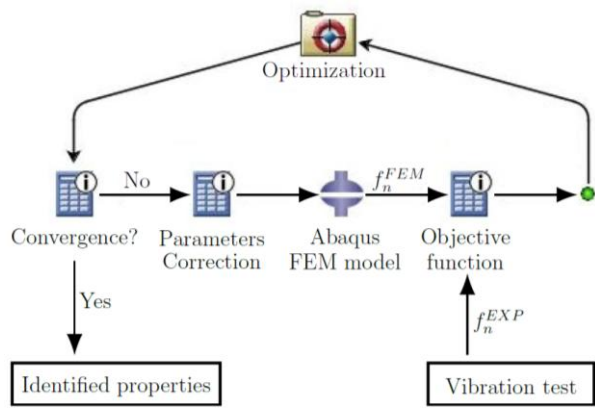
The proposed approach, while effective, has limitations that must be considered during the design process. It is specifically suited for thin, multi-layered plates and assumes linear elastic behaviour, making it appropriate only when deformations are small and the material response remains within the elastic range. As such, it does not account for nonlinear or viscoelastic effects, which may be relevant for polymer-based materials under large strains or time-dependent loading. Nonetheless, the linear elasticity assumption remains valid for many engineering applications involving thin-walled structures.

Tab. 4. Material properties.

Material	$E_1$ , [GPa]	$E_2$ , [GPa]	$G_{12}$ , [GPa]	$\nu_{12}$ , [-]	$\rho$ , [kg/m <sup>3</sup> ]
CF-PA-12	8.50	2.00	0.90	0.42	1030.00

Tab. 5. Optimal engineering constants for Plate 1.

Material	$E_1$ , [GPa]	$E_2$ , [GPa]	$G_{12}$ , [GPa]	$\nu_{12}$ , [-]
CF-PA-12	9.75	1.81	0.82	0.48



a)

b)

Fig. 9. a) Simulia/Isight inverse technique workflow; b) Objective function convergence history.

Tab. 6. Mode shapes of the Plate 2.

	Mode no.									
	1	2	3	4	5	6	7	8	9	10
Experiment										
FEM										

Tab. 7. Validation results for the Plate 2.

Resonance (n)	EXP*	FEM**	$\Delta$ [%]
	[Hz]		
	243.13	244.55	0.59
2	277.48	282.29	1.73
3	603.82	609.15	0.88
4	690.90	695.82	0.71
5	1008.80	1030.00	2.10
6	1080.69	1081.92	0.11
7	1164.58	1178.43	1.19
9	1357.01	1361.71	0.35
9	1560.16	1575.72	1.00
10	1739.57	1729.78	0.56
	Average		0.92

\* Average values from Tab. 3, relative error;

\*\* Calculated with optimal engineering constants (Tab.5)

## 5. Conclusions

The research presented in this study utilizes an inverse

## Acknowledgments

The current research has been supported by Polish National Agency for Academic Exchange (NAWA) under project “EU4DUAL4Ukraine”. no. BNI-UE-2023-5. The article was co-financed from the state budget of Poland and awarded by the Minister of Science within the framework of the Excellent Science II Programme.

technique to determine the elastic constants of individual layers in 3D-printed plates, combining experimental modal analysis with numerical simulations. The layered structure of 3D-printed plates was effectively modelled using Classical Laminated Plate Theory (CLPT), which provides a robust theoretical framework for predicting their linear dynamic response. The identified engineering constants are validated and ready for use in predicting the dynamic behaviour of plates with varying filament orientations across individual layers.

The findings of this research have significant implications for the design and optimization of 3D-printed composite materials. By employing a layered analysis grounded in laminated plate theory, engineers and materials scientists can achieve precise control over structural properties. This approach is particularly valuable in applications demanding engineered anisotropy – such as aerospace, automotive, and biomedical sectors – here material performance and reliability are essential.

## References

1. Oromiehie E, Prusty B G, Compston P, Rajan G. Automated fibre placement based composite structures: Review on the defects, impacts and inspections techniques. *Composite Structures* 2019; 224: 110987, <https://doi.org/10.1016/j.compstruct.2019.110987>.
2. Shirinzadeh B, Alici G, Foong C W, Cassidy G. Fabrication process of open surfaces by robotic fibre placement. *Robotics and Computer-Integrated Manufacturing* 2004; 20(1): 17-28, [https://doi.org/10.1016/S0736-5845\(03\)00050-4](https://doi.org/10.1016/S0736-5845(03)00050-4).
3. Somireddy M, Czekanski A, Singh C V. Development of constitutive material model of 3D printed structure via FDM. *Materials Today Communications* 2018; 15: 143-52, <https://doi.org/10.1016/j.mtcomm.2018.03.004>.
4. Somireddy M, Singh CV, Czekanski A. Analysis of the material behavior of 3D printed laminates via FFF. *Experimental Mechanics* 2019; 59(6): 871-81, <https://doi.org/10.1007/s11340-019-00511-5>.
5. Casavola C, Cazzato A, Moramarco V, Pappalettere C. Orthotropic mechanical properties of fused deposition modelling parts described by classical laminate theory. *Materials & Design* 2016; 90: 453-8, <https://doi.org/10.1016/j.matdes.2015.11.009>.
6. Rahmatabadi D, Soleyman E, Fallah Min Bashi M, Aberoumand M, Soltanmohammadi K, Ghasemi I, Baniassadi M, Abrinia K, Bodaghi M, Baghani M. 4D printing and annealing of PETG composites reinforced with short carbon fibers. *Physica Scripta* 2024; 99: 055957, <https://doi.org/10.1088/1402-4896/ad3b40>.
7. Pejkowski Ł, Seyda J, Nowicki K, Mrozik D. Mechanical performance of non-reinforced, carbon fiber reinforced and glass bubbles reinforced 3D printed PA12 polyamide. *Polymer Testing* 2023; 118: 107891, <https://doi.org/10.1016/j.polymertesting.2022.107891>.
8. Kohutiar M, Kakošová L, Krbata M, Janik R, Fekiač J J, Breznická A, Eckert M, Mikuš P, Timárová L. Comprehensive Review: Technological Approaches, Properties, and Applications of Pure and Reinforced Polyamide 6 (PA6) and Polyamide 12 (PA12) Composite Materials. *Polymers* 2025; 17(4): 442, <https://doi.org/10.3390/polym17040442>.
9. Ghasemi M, Mohammadpour M, Taheri-Behrooz F. Energy absorption and low-velocity impact responses of the sandwich panels with lattice truss core. *Journal of Sandwich Structures & Materials* 2024; 26(6): 793-811, <https://doi.org/10.1177/10996362241238272>.
10. Zou R, Xia Y, Liu S, Hu P, Hou W, Hu Q, Shan C. Isotropic and anisotropic elasticity and yielding of 3D printed material. *Composites Part B: Engineering* 2016; 99: 506-513, <https://doi.org/10.1016/j.compositesb.2016.06.009>.
11. Ahn S, Montero M, Odell D, Roundy S, Wright P K. Anisotropic material properties of fused deposition modeling ABS. *Rapid Prototyping Journal* 2002; 8(1): 248-257, <https://doi.org/10.1108/13552540210441166>.
12. Li L, Sun Q, Bellehumeur C, Gu P. Composite Modeling and Analysis for Fabrication of FDM Prototypes with Locally Controlled Properties. *Journal of Manufacturing Processes* 2002; 4(2): 129-141, [https://doi.org/10.1016/S1526-6125\(02\)70139-4](https://doi.org/10.1016/S1526-6125(02)70139-4).
13. Anitha R, Arunachalam S, Radhakrishnan P. Critical parameters influencing the quality of prototypes in fused deposition modeling. *Journal of Materials Processing Technology* 2001; 118(1): 385-388, [https://doi.org/10.1016/S0924-0136\(01\)00980-3](https://doi.org/10.1016/S0924-0136(01)00980-3).
14. Kulkarni P, Dutta D. Deposition Strategies and Resulting Part Stiffnesses in Fused Deposition Modeling. *Journal of Manufacturing Science and Engineering* 1999; 121(1): 93-103, <https://doi.org/10.1115/1.2830582>.
15. Jiang D, Smith D E. Anisotropic mechanical properties of oriented carbon fiber filled polymer composites produced with fused filament fabrication. *Additive Manufacturing* 2017; 18: 84-94, <https://doi.org/10.1016/j.addma.2017.08.006>.
16. Fang G, Zhang T, Huang Y, Zhang Z, Masania K, Wang C. Exceptional mechanical performance by spatial printing with continuous fiber: Curved slicing, toolpath generation and physical verification. *Additive Manufacturing* 2024; 82: 104048, <https://doi.org/10.1016/j.addma.2024.104048>.
17. Volgin O, Shishkovsky I V. Material modelling of FDM printed PLA part. *Engineering Solid Mechanics* 2021; 9: 153-160, <http://doi.org/10.5267/j.esm.2020.12.004>.
18. Scapin M, Peroni L. Numerical Simulations of Components Produced by Fused Deposition 3D Printing. *Materials* 2021; 14: 4625; <https://doi.org/10.3390/ma14164625>.
19. Somireddy M, Czekanski A. Computational modeling of constitutive behaviour of 3D printed composite structures. *Journal of Materials Research and Technology* 2021; 11: 1710-1718, <https://doi.org/10.1016/j.jmrt.2021.02.030>.
20. Nasirov A, Fidan I. Prediction of mechanical properties of fused filament fabricated structures via asymptotic homogenization. *Mechanics of Materials* 2020; 145: 103372, <https://doi.org/10.1016/j.mechmat.2020.103372>.
21. Cuan-Urquizo E, Barocio E, Tejada-Ortigoza V, Pipes R B, Rodriguez C A, Roman-Flores A. Characterization of the Mechanical Properties

- of FFF Structures and Materials: A Review on the Experimental, Computational and Theoretical Approaches. *Materials* 2019; 12(6): 895, <https://www.mdpi.com/1996-1944/12/6/895>.
22. Frederiksen P S. Experimental procedure and results for the identification of elastic constants of thick plates. *Journal of Composite Materials* 1997; 31(4): 360-382, <https://doi.org/10.1177/002199839703100403>.
  23. Lauwagie T, Sol H, Roebben G, Heylen W, Shi Y, Van der Biest O. Mixed numerical–experimental identification of elastic properties of orthotropic metal plates. *NDT & E International* 2003; 36(7): 487-495, [https://doi.org/10.1016/S0963-8695\(03\)00048-3](https://doi.org/10.1016/S0963-8695(03)00048-3).
  24. Wesolowski M, Barkanov E. Improving material damping characterization of a laminated plate. *Journal of Sound and Vibration* 2019; 462: 114928, <https://doi.org/10.1016/j.jsv.2019.114928>.
  25. Mota Soares C M, Moreira de Freitas M , Araújo A L, Pedersen P. Identification of material properties of composite plate specimens. *Composite Structures* 1993; 25(1): 277-285, [https://doi.org/10.1016/0263-8223\(93\)90174-O](https://doi.org/10.1016/0263-8223(93)90174-O).
  26. Araújo A L, Mota Soares C M, Moreira de Freitas M. Characterization of material parameters of composite plate specimens using optimisation an experimental vibration data. *Composites Part B: Engineering* 1996; 27(2): 185-191, [https://doi.org/10.1016/1359-8368\(95\)00050-X](https://doi.org/10.1016/1359-8368(95)00050-X).
  27. Rikards R, Chate A, Steinchen W, Kessler A, Bledzki A K. Method for identification of elastic properties of laminates based on experiment design. *Composites Part B: Engineering* 1999; 30(3): 279-289, [https://doi.org/10.1016/S1359-8368\(98\)00059-6](https://doi.org/10.1016/S1359-8368(98)00059-6).
  28. Rikards R, Chate A, Gailis G. Identification of elastic properties of laminates based on experiment design. *International Journal of Solids and Structures* 2001; 38(3): 5097-5115, [https://doi.org/10.1016/S0020-7683\(00\)00349-8](https://doi.org/10.1016/S0020-7683(00)00349-8).
  29. Jones R M. *Mechanics of Composite Materials*. Second Edition. Taylor & Francis: 1999.
  30. Reddy J N. *Mechanics of Laminated Composite Plates and Shells. Theory and Analysis*. Second Edition. CRC Press LLC: 2004. <https://doi.org/10.1201/b12409>
  31. Hooke R, Jeeves T A. “Direct Search” Solution of Numerical and Statistical Problems. *Journal of the Association for Computing Machinery* 1961; 8(2): 212-229, <https://doi.org/10.1145/321062.321069>.
  32. POLYTEC Hardware Manual, 2008.
  33. Ewins D J. *Modal Testing: Theory, Practice and Application// Second Edition*. – Research Studies Press LTD, 2000.
  34. ASTM C393/C393M-20. American Society for Testing and Materials Standards, Standard Test Method for Core Shear Properties of Sandwich Constructions by Beam Flexure, 2020.